Editors' Suggestion

Imaginary Gauge Potentials in a Non-Hermitian Spin-Orbit Coupled Quantum Gas

J. Tao,[1,2,*] E. D. Mercado-Gutierrez,[1,*] M. Zhao,[1] and I. B. Spielman[1,†]

[1]Joint Quantum Institute, University of Maryland and National Institute of Standards and Technology, College Park, Maryland 20742, USA

[2]Department of Physics, Harvard University, Cambridge, Massachusetts 02138, USA

(Received 25 May 2025; revised 4 January 2026; accepted 13 February 2026; published 17 March 2026)

In 1996, Hatano and Nelson proposed a non-Hermitian lattice model containing an imaginary Peierls phase [Phys. Rev. Lett. 77, 570 (1996)], which subsequent analyses revealed to be an instance of a new class of topological systems. Here, we experimentally realize a continuum analog to this model containing an imaginary gauge potential using a homogeneous spin-orbit coupled Bose-Einstein condensate (BEC). Non-Hermiticity is introduced by adding tunable spin-dependent loss via microwave coupling to a subspace with spontaneous emission. We demonstrate that the resulting Heisenberg equations of motion for position and momentum depend explicitly on the system's phase-space distribution. First, we observe collective nonreciprocal transport in real space, with a "self-acceleration" that decreases with the BEC's spatial extent, consistent with non-Hermitian Gross-Pitaevskii simulations. We then examine localized edge states: the relatively strong interactions in our BEC suppress the formation of topological edge states, yielding instead highly excited states localized by an interplay between self-acceleration and wave function spreading. Finally, we confirm that our non-Hermitian description remains valid at all times by comparing it to a multilevel master equation treatment.

DOI: 10.1103/tpfc-n3bq

Open quantum systems are characterized by an interplay between their closed system dynamics and those resulting from the external reservoir. Because this evolution goes beyond what is possible in closed systems, open systems offer new opportunities and paradigms for quantum engineering [1–3]. In some limits, this evolution can be described by effective non-Hermitian Hamiltonians with unusual spectral features such as singular exceptional points [4–8] and phases characterized by spectral topology [5,9,10]. The Hatano-Nelson (HN) model [11,12] describes a non-Hermitian lattice with a constant imaginary Peierls phase with topology quantified by an integer winding number [5,9,13]. The resulting non-Hermitian skin effect (NHSE) [14,15] has been observed for noninteracting particles in a range of experimental platforms [16–20]. By contrast with a uniform real-valued Peierls phase, which can be eliminated by a gauge transformation, its imaginary counterpart has direct physical consequences such as nonreciprocal wavefunction localization [11,14,17–19,21] and an equivalent description of evolution on curved space [22,23].

We experimentally studied an interacting atomic Bose-Einstein condensate (BEC), the continuum analog subject to the (disorder free) HN model in real space. This model features a spatially uniform imaginary gauge potential with single-particle non-Hermitian Hamiltonian,

$$\hat{H}_{\mathrm{nh}} = \frac{(\hat{p} - i\mathcal{B})^2}{2m^*} + V(\hat{x}) - i\hbar\frac{\gamma}{2}, \tag{1}$$

with effective mass m^*, canonical momentum $\hat{p}$, imaginary gauge potential $\mathcal{B}$, external potential V, and, since there is no gain in our atomic BEC, an overall loss rate γ. We introduced $\mathcal{B}$ into atomic BECs by combining laser-induced spin-orbit coupling (SOC) and spin-dependent loss. As shown in Figs. 1(a) and 1(b), a pair of lasers Raman coupled two internal states $|\downarrow\rangle$ and $|\uparrow\rangle$ with strength Ω, recoil momentum p_0 [24], and recoil energy $\hbar\omega_0 = p_0^2/(2m)$; an additional microwave field drove transitions between $|\uparrow\rangle$ and a lossy "reservoir" subspace. This gives rise to a two-band non-Hermitian SOC model with a Hamiltonian,

$$\hat{H}_{\mathrm{SOC}} = \frac{(\hat{p} + p_0\sigma_z)^2}{2m} + \frac{\hbar\Omega}{2}\sigma_x + \frac{\hbar\delta}{2}\sigma_z - i\hbar\gamma\mathcal{P}_{\uparrow}, \tag{2}$$

in terms of Pauli operators $\sigma_{x,y,z}$, quasimomentum $\hat{p}$ [25], atomic mass m, detuning δ, and the spin projection operator $\mathcal{P}_{\uparrow} = |\uparrow\rangle\langle\uparrow|$.

*These authors contributed equally to this work.

†Contact author: ian.spielman@nist.gov

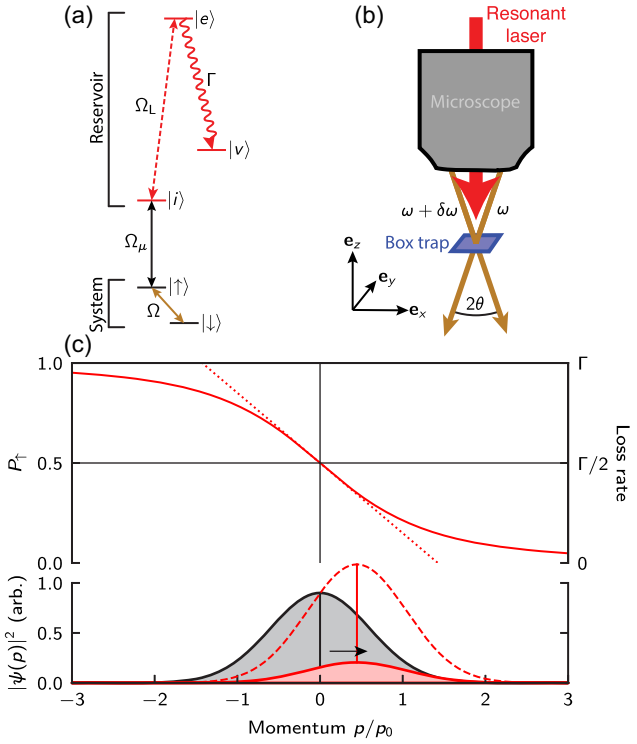

FIG. 1. Concept. (a) Level diagram for creating non-Hermitian SOC in a system subspace linked to a reservoir subspace with a microwave field of strength Ω_μ. Dissipation is induced when the excited state $|e\rangle$ decays with rate Γ. (b) Geometry. A homogeneous BEC was confined in a box-shaped trap in the $\mathbf{e}_x$-$\mathbf{e}_y$ plane and Raman dressed by a pair of laser beams projected through a high-resolution microscope objective. Dissipation is induced by a resonant laser. (c) Imaginary gauge potential. Left: spin up population and imaginary gauge field as a function of momentum (solid) along with their linear approximations (dashed). Right: corresponding momentum dependent loss. Both computed for $\Omega/\omega_0 = 5.7$. Bottom: Gaussian momentum distribution before (black) and accelerated after (red) evolving with $\gamma = 0.19\omega_0$ for 10 ms. The solid red curve plots the final distribution including the overall loss term in Eq. (1), while the dashed curve includes only the imaginary gauge potential.

We make an adiabatic approximation in which dynamics are projected into the lowest band and focus on the large Raman coupling ($\Omega > 4\omega_0$) "single minimum" limit, where the Hermitian contribution to $\hat{H}_{\mathrm{SOC}}$ has low-energy dynamics well described by the effective mass m^* [26]. The ground state, a plane wave at $p = 0$, consists of an equal superposition of $|\uparrow\rangle$ and $|\downarrow\rangle$; for eigenstates with $p \ll \sqrt{2m\hbar\Omega}$, the occupation probabilities are proportional to p with $P_{\uparrow,\downarrow}(p) = [1 \mp 2p_0 p/(m\hbar\Omega)]/2$. As can be seen in Fig. 1(c), these probabilities lead to a lowest band non-Hermitian contribution to Eq. (2) of $-i\hbar\gamma P_\uparrow(\hat{p})$, equivalent to an imaginary gauge field,

$$\mathcal{B} = -p_0 \frac{\gamma}{\Omega - 4\omega_0}, \tag{3}$$

along with an overall loss rate $\gamma/2$ (in what follows, we will omit this straightforward contribution). These expressions are suitable for our experimental configuration [47].

Setup—We realized this configuration for nearly pure ^{87}Rb BECs (with $N_0 \approx 2 \times 10^5$ atoms and chemical potential $\mu \approx h \times 500$ Hz) confined by the joint action of blue and red detuned optical dipole traps (ODTs, with wavelengths 635 and 1064 nm, respectively). The blue ODT horizontally confined the BEC in a $L = 30$ μm square (in the $\mathbf{e}_x$-$\mathbf{e}_y$ plane, projected using a numerical aperture NA = 0.55 microscope) while the red ODT provided a vertically oriented ($\mathbf{e}_z$) harmonic potential with frequency $\omega_z/(2\pi) \approx 220$ Hz, as well as a $\omega_y/(2\pi) \approx 30$ Hz contribution to the trap along $\mathbf{e}_y$. Our experiments focused on the state space spanned by $|f = 1, m_F = 0\rangle$ and $|f = 1, m_F = 1\rangle$ that served as our spin states $|\uparrow\rangle$ and $|\downarrow\rangle$, respectively. A large bias magnetic field $B_0 \approx 978$ μT along $\mathbf{e}_y$ provided sufficient quadratic contribution to the Zeeman shift for us to resonantly couple $|\uparrow\rangle$ and $|\downarrow\rangle$ while being far off resonance to $|f = 1, m_F = -1\rangle$. As seen in Fig. 1(a), we induced spin-orbit coupling with strength $p_0 = (2\pi\hbar/\lambda_R) \times \sin(\theta)$ by Raman coupling $|\uparrow\rangle$ and $|\downarrow\rangle$ with a pair of $\lambda_R = 790.03$ nm laser beams intersecting with half-angle $\theta = 16.5$ degrees giving $\omega_0/(2\pi) \approx 300$ Hz and prepared the SOC ground state (see Methods). The spin-dependent loss in Eq. (2) was created by simultaneously microwave coupling $|\uparrow\rangle$ (with Rabi frequency Ω_μ) to an intermediate electronic ground state $|i\rangle = |f = 2, m_F = 0\rangle$ while expelling atoms with a laser resonant between $|i\rangle$ and the $|f' = 3, m'_F = 0\rangle$ excited state. This laser, aligned along $\mathbf{e}_z$, had intensity I and optical Rabi frequency $\Omega_{\mathrm{L}} = \Gamma\sqrt{I/(2I_{\mathrm{sat}})}$ in terms of the natural linewidth Γ and saturation intensity $\mathrm{I}_{\mathrm{sat}}$ [27]. We chose Ω_μ and Ω_{L} to minimize the instantaneous occupation of the $f = 2$ manifold, thereby mitigating density-dependent optical effects [28].

Dynamical evolution—We begin by considering the dynamics of Hermitian observables. Reference [29] showed that the response to general non-Hermitian Hamiltonians can be exotic and very different from their Hermitian counterparts. Subject to non-Hermitian gauge field $\mathcal{B}$, the Heisenberg equation of motion (EoM) for an operator $\hat{o}$ becomes

$$i\hbar\partial_t\langle\hat{o}\rangle = \langle[\hat{o}, \hat{H}_{\mathrm{h}}]\rangle - \frac{i\mathcal{B}}{m^*}\langle\{\delta\hat{p}, \delta\hat{o}\}\rangle, \tag{4}$$

where $\delta\hat{o} \equiv \hat{o} - \langle\hat{o}\rangle$ and $\hat{H}_{\mathrm{h}}$ is the Hermitian contribution to $\hat{H}_{\mathrm{nh}}$ [47]. For example, this implies that the EoM for momentum $i\hbar\partial_t\langle\hat{p}\rangle = \langle[\hat{p}, \hat{V}]\rangle - 2i\mathcal{B}\langle\delta\hat{p}^2\rangle/m^*$ (i.e., the force equation) directly depends on the variance of the momentum distribution $\langle\delta\hat{p}^2\rangle$. The physical origin of this "self-acceleration" can be understood by considering the free evolution of a Gaussian wave packet in momentum

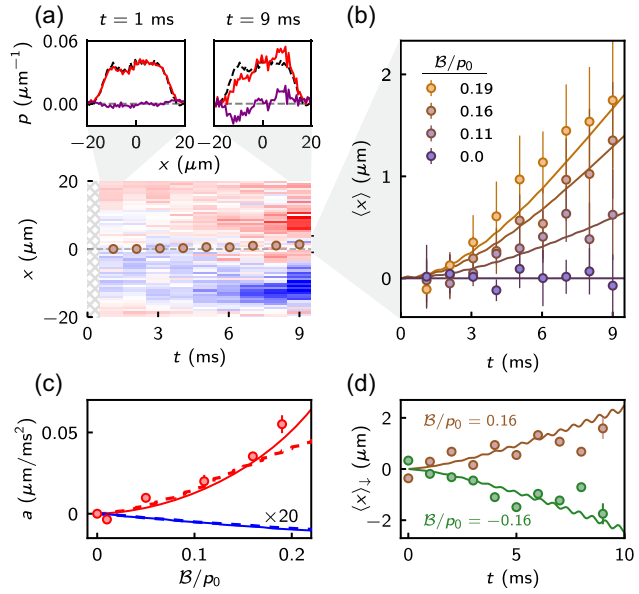

FIG. 2. Nonreciprocal transport. (a) Time dependence of 1D atomic density at $\mathcal{B}/p_0 = 0.16$. Top: density profiles at $t = 1$ and $t = 9$ ms (red) along with the $t = 0$ profile (black dashed) and their difference Δn (purple). Bottom: Δn as function of evolution time along with the measured c.m. position (markers). In (b)–(d), markers are experimental data, and solid curves are GPE simulations. (b) Center of mass time evolution for a range of $\mathcal{B}/p_0$. Each point reflects the average of about 10 measurements, and the uncertainties are the standard error of the mean. (c) Initial acceleration as a function of $\mathcal{B}/p_0$. Markers result from fits to the experimental data in (a); solid curves are simulated acceleration with (red) and without (blue, magnified by 20×) atomic interactions. Dashed curves plot the corresponding EoM-predicted acceleration averaged for the first 6 ms. (d) Reversed gauge field. Single spin transport $\langle x\rangle_\downarrow$ at $|\mathcal{B}/p_0| = 0.16$.

space, with the initial state shown by the black curve in Fig. 1(c), bottom. The anti-Hermitian contribution to the Hamiltonian, $-i\hat{p}\mathcal{B}/m^*$, gives a time evolution operator $\hat{U}_{\rm ah} = \exp[-p\mathcal{B}t/(\hbar m^*)]$ that includes loss for $p > 0$ and gain for $p < 0$. As shown by the red curves (with dashes including only the imaginary vector potential and solid adding the overall loss term $\gamma/2$), the action of this operator shifts the centroid by $-2\mathcal{B}\Delta p^2 t/(\hbar m^*)$ (where Δp is the initial width of the distribution), as expected from the force equation.

In a similar manner, the EoM for the center-of-mass (c.m.) position is given by $i\hbar\partial_t\langle\hat{x}\rangle = i\hbar\langle\hat{p}\rangle/m^* - i\mathcal{B}\langle\{\delta\hat{p}, \delta\hat{x}\}\rangle/m^*$, indicating that the c.m. dynamics are influenced not only by the canonical momentum $\langle\hat{p}\rangle$ but also by an additional anomalous term. This "self-displacement" term arises from the imaginary gauge field interacting with correlated fluctuations in momentum and position.

While these EoMs effectively isolate the role of the imaginary gauge potential in dynamics, they are difficult to employ for predicting dynamics: the equations for $\langle\hat{x}\rangle$ and $\langle\hat{p}\rangle$ are not closed. That is, they involve an infinite hierarchy of coupled equations describing ever higher order anticommutators and operator products. For example, computing the acceleration demands the time derivative $\partial_t\langle\{\delta\hat{p}, \delta\hat{x}\}\rangle$. Using Eq. (4) together with the kinetic and force equations, we obtain

$$\hbar\partial_t^2\langle\hat{x}\rangle = i\frac{\langle[\hat{V},\hat{p}]\rangle}{m^*} - \frac{4\mathcal{B}}{(m^*)^2}\langle\delta\hat{p}^2\rangle + i\frac{\mathcal{B}}{m^*}\langle\{\delta\hat{x},[\hat{V},\hat{p}]\}\rangle + \ldots, \tag{5}$$

which is only valid for short times [47].

Nonreciprocal transport—After preparing the BEC in the SOC ground state, we simultaneously applied the microwave and optical fields and allowed the system to evolve for up to 9 ms. Using the high NA microscope pictured in Fig. 1(b), we separately measured the *in situ* $|\uparrow\rangle$ and $|\downarrow\rangle$ density distributions via partial transfer absorption imaging [30] and obtained the total density from their sum [Fig. 2(a), top]. As time progresses, a clearly visible displacement develops in the differential density $\Delta n(t) = n(t) - n(0)$, leading to the small shift in $\langle x\rangle$ [markers in Fig. 2(a), bottom). The expanded view in Fig. 2(b) shows that the c.m. initially evolves proportionally to t^2. We extracted the acceleration from quadratic fits to the early time dynamics (up to 9 ms) and plot it as a function of the imaginary gauge potential $\mathcal{B}/p_0$ in Fig. 2(c) derived from observed loss rate γ with Eq. (3). The solid blue curve, representing the acceleration predicted by the non-interacting Hamiltonians thus far discussed, bears no resemblance to our data.

Going beyond this description, our BEC also has interactions that are described by the Gross-Pitaevskii equation (GPE). This effectively augments the Hamiltonian with a mean field energy $g|\psi(x)|^2$, which is proportional to the local atomic density $|\psi(x)|^2$ and an interaction strength g. For our experimental parameters, GPE simulations of the continuum HN model [Eq. (1)] are in agreement with those of full two-band SOC Hamiltonian [Eq. (2)]; therefore, wherever possible, we compare our experimental data to the suitable interacting continuum HN model.

The solid curves in Fig. 2(b) represent GPE simulations of our experiment performed with no adjustable parameters and show excellent agreement with our observations. Likewise, the GPE-predicted acceleration [solid red curve in Fig. 2(c)] also closely matches our measured data. Additionally, the dashed curves confirm that the closed-form expression for the short-time acceleration [Eq. (5)] is valid for both the noninteracting and interacting cases [i.e., using $V \to V + g|\psi|^2$ in Eq. (5)] up to $\mathcal{B}/p_0 \approx 0.18$, beyond which higher order terms become non-negligible [47].

The stark contrast between the single-particle and GPE accelerations arise from the markedly different spatial

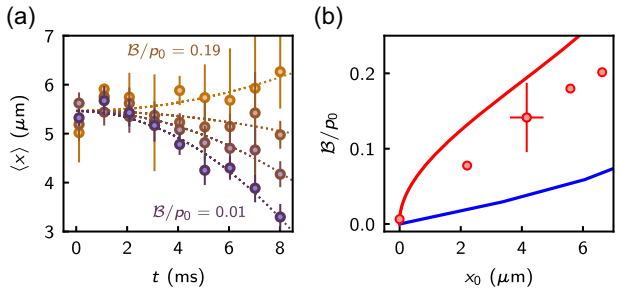

FIG. 3. Dynamical edge modes. (a) c.m. dynamics of an initially canted state for a range of $\mathcal{B}$ (markers) along with quadratic fits (dashed curves), with $\mathcal{B}/p_0 = 0.19$, 0.11, 0.05, 0.01 (top to bottom). (b) Optimal $\mathcal{B}/p_0$ from data as in (a) versus c.m. position x_0 (markers, single error bar is representative of all data). Curves show calculations with (red) and without (blue) interactions.

modes of these two cases. On one hand, the noninteracting particle in a box has a cosinusoidal ground state $\propto \cos(\pi x/L)$ that is hardly affected by the 0.9 μm box-trap projection resolution. On the other hand, the BEC wave function remains essentially uniform until it drops rapidly to zero at the box edge over a length scale determined by an interplay of the $\xi \approx 0.3$ μm healing length and the NA-limited sharpness of the trap's edge. This interaction-driven change enhances both the self-acceleration and self-displacement contributions to the $\langle \hat{p} \rangle$ and $\langle \hat{x} \rangle$ EoMs. Because both ξ and the projection resolution are much smaller than L, the interacting system's momentum-space wave function is broadened, thereby enhancing the self-acceleration $\propto \langle \hat{p}^2 \rangle$. Furthermore, interactions extend the wave function into regions where the trap potential varies rapidly, amplifying the self-displacement contribution $\propto \langle \{\delta\hat{x}, [\hat{V}, \hat{p}]\} \rangle$ and, thus, increasing the acceleration.

Thus far, we have modified only the magnitude of the imaginary gauge potential $\mathcal{B}$ (which is $\propto \gamma$); this is because in our loss-only system the decay rate γ is strictly positive, so changes to it cannot affect the sign of $\mathcal{B}$.

To invert the sign of $\mathcal{B}$, we coupled $|\downarrow\rangle$ rather than $|\uparrow\rangle$ to the lossy subspace, thereby replacing $\mathcal{P}_\uparrow$ with $\mathcal{P}_\downarrow$ in Eq. (2) and flipping the sign of $\mathcal{B}$ in Eq. (3) [31]. Figure 2(d) illustrates the effect of this change: because both the self-acceleration and self-displacement are $\propto \mathcal{B}$, reversing its sign inverts the nonreciprocal transport. Unlike in Figs. 2(a)–2(c), we now focus on $\langle x \rangle_\downarrow$, the c.m. position of only the $|\downarrow\rangle$ spin state. We do so for two reasons: first, this component's displacement is increased relative to the average yielding a larger signal, and second predicting spin-resolved motion requires the full two-band SOC. The data are consistent within uncertainties with the result of this two-band GPE calculation (solid curves); however, the simulation exhibits high-frequency oscillations, resulting from coherent oscillations between the two SOC bands. These confirm that small deviations from the single-band (adiabatic) approximation exist but remain undetectable within our current experimental sensitivity.

Suppressed non-Hermitian skin effect—Both non-Hermitian terms—$i\mathcal{B}$ and $i\hbar\gamma/2$—can be eliminated from Eq. (1) by an "antiunitary gauge transformation," $\hat{A} = \exp(\mathcal{B}\hat{x}/\hbar - \gamma t/2)$. The transformed wave function $|\psi'\rangle = \hat{A}|\psi\rangle$ obeys the usual Schrödinger equation, making it straightforward to compute and understand eigenstates and dynamics. For example, the noninteracting ground state immediately leads to the non-Hermitian solution $\propto \cos(\pi x/L)\exp(-\mathcal{B}x/\hbar)$; this state, exponentially localized to the boundary, directly manifests the NHSE [32].

Expecting a similar outcome for our homogeneously trapped BEC, we prepared BECs with an initially "canted" density distribution and then abruptly switched γ to a nonzero value. Figure 3(a) shows that the c.m. position undergoes uniform acceleration that depends systematically on $\mathcal{B}$; the dashed curves are quadratic fits that yield the acceleration. From the zero crossing of this acceleration, we identify the value of $\mathcal{B}$ with no net motion. Data of this type, collected using different initial c.m. positions, are shown in Fig. 3(b). It might be tempting to interpret these configurations as equilibrium NHSE states; however, they deviate markedly from the single-particle solution (blue).

Indeed, applying the antiunitary gauge transformation to the GPE shows that our system's ground state is expected to be described by a Thomas-Fermi-like uniform density distribution, leaving only small vestiges of the NHSE at the BEC's low-density periphery [33]. In line with recent theory [34–36], our numerics show that the c.m. displacement of the GPE ground state is nonzero, but it isgreatly reduced compared to the noninteracting case, owing to the interaction energy cost of changing the ground state mode.

The red curve in Fig. 3(a) plots the results of a full time-dependent GPE simulation, showing significantly improved agreement with experiment. These simulations show that the observed "static" configuration is actually a dynamical effect—somewhat analogous to macroscopic self-trapping [37] of BECs in double-well potentials—here the effects of self-acceleration and self-displacement are counterbalanced by the BECs repulsive interactions.

Validity of method—The behavior of open quantum systems—governed by the quantum master equation—can be approximated by non-Hermitian Hamiltonians only up to the first so-called quantum jump, which, for the data presented here, occurs in about twice the 26 ns lifetime of ^{87}Rb's $5P_{3/2}$ excited state. Nevertheless, we observe non-Hermitian evolution on millisecond timescales, raising an immediate question: how can a non-Hermitian picture remain valid for such long durations?

We experimentally explored this question in a simplified configuration using rf rather than Raman to induce $|\uparrow\rangle \leftrightarrow |\downarrow\rangle$ coupling [38]. Beginning with a $|\uparrow\rangle$ BEC, we abruptly applied combinations of optical, microwave, and rf fields

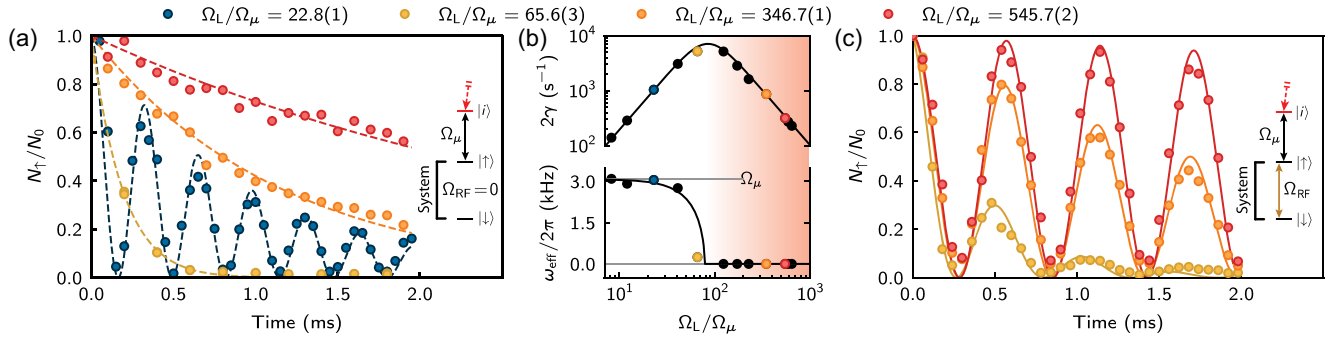

FIG. 4. Transition from coherent to quantum Zeno regime. (a) Data with $\Omega_{\rm RF} = 0$ showing fractional population in $|\uparrow\rangle$ versus time for four values of $\Omega_{\rm L}$, all with $\Omega_\mu = 2\pi \times 3.08(4)$ kHz. Solid curves are fits as described in the text. (b) Lifetime and oscillation frequency extracted from the fits as in (a), plotted as a function of $\Omega_{\rm L}/\Omega_\mu$. Solid curves result from time-domain master equation simulations (no free parameters), with $\omega_{\rm eff}$ and γ obtained from fits as in (a). (c) Fractional population in $|\uparrow\rangle$ versus time, now with rf coupling $\Omega_{\rm RF} = 2\pi \times 1.20(5)$ kHz. Solid curves show the predictions of the non-Hermitian Hamiltonian (no free parameters).

for a duration t, and monitored the time-evolving populations $N_\uparrow$, $N_\downarrow$, and N_i.

We begin with the minimal scenario of no rf coupling (i.e., $\Omega_{\rm RF} = 0$), illustrated in Fig. 4(a), where the system state space is just $|\uparrow\rangle$. The markers show the time evolution of the normalized population $N_\uparrow/N_0$ for a range of optical Rabi frequencies Ω_L. When $\Omega_{\rm L}/\Omega_\mu \ll 1$, the system exhibits damped Rabi oscillations between $|\uparrow\rangle$ and $|i\rangle$, while for $\Omega_{\rm L}/\Omega_\mu \gg 1$, the evolution instead yielded simple exponential decay. In a standard three-level master equation description, a quantum jump (spontaneous decay) returns the atom from $|e\rangle$ to $|i\rangle$, at which time the non-Hermitian approximation fails. In our shallow trap, however, the recoil momentum imparted during spontaneous decay ejects the atom so that it never returns, effectively removing any jumped atoms from observation. This mechanism resolves the question: no observed atom has undergone a quantum jump, making a non-Hermitian description possible for all times.

The resulting non-Hermitian Hamiltonian for the reduced system subspace, $\hat{H}_{\rm min} = -i\hbar\gamma\mathcal{P}_\uparrow$, predicts exponential decay (with rate 2γ) and, therefore, requires $\Omega_{\rm L}/\Omega_\mu \gg 1$. The dashed curves in Fig. 4(a) show fits describing damped oscillatory behavior via $\exp(-2\gamma t)\cos^2(\omega_{\rm eff}t/2)$ to our data. Figure 4(b) collects the results of such fits (markers) and compares them with parameters obtained from master equation simulations featuring quantum jumps only from $|e\rangle$ to $|v\rangle$ (curves, computed with no free parameters). In both cases, the oscillation frequency drops to zero when $\Omega_{\rm L} = 2\Omega_\mu$, marking a sharp transition from damped oscillations to exponential decay. In the exponential-decay regime (shaded), γ decreases with increasing $\Omega_{\rm L}$, manifesting the quantum Zeno effect [39].

These data fully calibrate the non-Hermitian contribution to the system Hamiltonian. To verify this calibration, we introduce rf coupling in the Zeno regime [Fig. 4(c)] and compare the observed dynamics with the predictions of our non-Hermitian model (solid curves). No free parameters are used: the decay rates come from Fig. 4(b), and the rf Rabi frequency was independently measured. Our results, thus, confirm that the non-Hermitian description is quantitatively accurate beyond the nominal quantum jump timescale.

Discussion and outlook—Here we realized an imaginary gauge potential using a spin-orbit coupled BEC with laser-induced loss and demonstrated that such a framework can be valid for all times. This implementation serves as a specific example of a more general scenario [40], in which a subspace $|S\rangle$, evolving under otherwise Hamiltonian evolution, experiences quantum jumps into an uncoupled subspace $|V\rangle$.

In our system, repulsive interactions have the apparently contradictory effects of enhancing self-acceleration while simultaneously suppressing the NHSE; this naturally raises questions about the impact of these mean field interactions on spectral topology and the non-Hermitian bulk-boundary correspondence. While our results focused on c.m. variables, the underlying GPE simulations show that this is accompanied by the formation of rapidly oscillatory shock waves, with the wavelength below our imaging resolution. These patterns are reminiscent of those predicted in the context of non-Hermitian analog gravity simulations [41].

Originally Hatano and Nelson initially considered an interplay between Hermitian disorder and an imaginary gauge potential [11]; this configuration can easily be realized in cold-atom experiments. Moreover, by patterning the loss, beam disorder can be added to the imaginary gauge potential [42,43]. Moving beyond simple single-particle or mean field descriptions introduces core conceptual questions because loss and gain reflect transitions between Fock spaces of the total atom number, rather than simply modifying the wave function normalization. In this context, defining non-Hermitian many-body topological invariants is a key challenge [34,35]. Despite these challenges, new strongly correlated physics is predicted in non-Hermitian quantum systems. For instance, asymmetric fermionization dynamics have been theorized in the Tonks-Girardeau

regime of the 1D Bose gas [44]. In lattice systems, combining nonreciprocal hopping with Hubbard interactions may stabilize novel phases, such as non-Hermitian Mott insulators and many-body localized states [34–36,45].

Acknowledgments—The authors thank R. Ravi and K. Weber for carefully reading the manuscript, as well as Q. Zhou and W. Xu for stimulating discussions. This work was partially supported by the National Institute of Standards and Technology; the Quantum Leap Challenge Institute for Robust Quantum Simulation (No. OMA-2120757); and the Air Force Office of Scientific Research Multidisciplinary University Research Initiative "RAPSYDY in Q" (No. FA9550-22-1-0339).

J. T. and E. D. M.-G. conducted the experiment, performed theoretical work, and analyzed data; J. T., E. D. M.-G., and M. Z. developed, implemented, and maintained the experimental apparatus. J. T. and E. D. M.-G. conceived of the experiment with input from I. B. S.; I. B. S. provided mentorship and obtained funding. All authors substantially participated in the discussion and the writing of the manuscript.

The authors declare that they have no competing financial interests.

Data availability—The data that support the findings of this article are openly available [46].

[1] W. Happer, Optical pumping, Rev. Mod. Phys. **44**, 169 (1972).
[2] H. J. Briegel, D. E. Browne, W. Dür, R. Raussendorf, and M. Van den Nest, Measurement-based quantum computation, Nat. Phys. **5**, 19 (2009).
[3] B. M. Terhal, Quantum error correction for quantum memories, Rev. Mod. Phys. **87**, 307 (2015).
[4] M.-A. Miri and A. Alu, Exceptional points in optics and photonics, Science **363**, eaar7709 (2019).
[5] Y. Ashida, Z. Gong, and M. Ueda, Non-Hermitian physics, Adv. Phys. **69**, 249 (2020).
[6] E. J. Bergholtz, J. C. Budich, and F. K. Kunst, Exceptional topology of non-Hermitian systems, Rev. Mod. Phys. **93**, 015005 (2021).
[7] Z. Ren, D. Liu, E. Zhao, C. He, K. K. Pak, J. Li, and G.-B. Jo, Chiral control of quantum states in non-Hermitian spin–orbit-coupled fermions, Nat. Phys. **18**, 385 (2022).
[8] Y.-J. Liu, K. K. Pak, P. Ren, M. Guo, E. Zhao, C. He, and G.-B. Jo, Third-order exceptional point in non-Hermitian spin-orbit-coupled cold atoms, Phys. Rev. A **112**, 023305 (2025).
[9] K. Kawabata, K. Shiozaki, M. Ueda, and M. Sato, Symmetry and topology in non-Hermitian physics, Phys. Rev. X **9**, 041015 (2019).
[10] K. Wang, A. Dutt, C. C. Wojcik, and S. Fan, Topological complex-energy braiding of non-Hermitian bands, Nature (London) **598**, 59 (2021).
[11] N. Hatano and D. R. Nelson, Localization transitions in non-Hermitian quantum mechanics, Phys. Rev. Lett. **77**, 570 (1996).
[12] N. Hatano and D. R. Nelson, Vortex pinning and non-Hermitian quantum mechanics, Phys. Rev. B **56**, 8651 (1997).
[13] K. Zhang, Z. Yang, and C. Fang, Correspondence between winding numbers and skin modes in non-Hermitian systems, Phys. Rev. Lett. **125**, 126402 (2020).
[14] S. Yao and Z. Wang, Edge states and topological invariants of non-Hermitian systems, Phys. Rev. Lett. **121**, 086803 (2018).
[15] F. Song, S. Yao, and Z. Wang, Non-Hermitian skin effect and chiral damping in open quantum systems, Phys. Rev. Lett. **123**, 170401 (2019).
[16] Q. Liang, D. Xie, Z. Dong, H. Li, H. Li, B. Gadway, W. Yi, and B. Yan, Dynamic signatures of non-Hermitian skin effect and topology in ultracold atoms, Phys. Rev. Lett. **129**, 070401 (2022).
[17] X. Zhang, Y. Tian, J.-H. Jiang, M.-H. Lu, and Y.-F. Chen, Observation of higher-order non-Hermitian skin effect, Nat. Commun. **12**, 5377 (2021).
[18] L. Xiao, T. Deng, K. Wang, G. Zhu, Z. Wang, W. Yi, and P. Xue, Non-Hermitian bulk–boundary correspondence in quantum dynamics, Nat. Phys. **16**, 761 (2020).
[19] S. Weidemann, M. Kremer, T. Helbig, T. Hofmann, A. Stegmaier, M. Greiter, R. Thomale, and A. Szameit, Topological funneling of light, Science **368**, 311 (2020).
[20] E. Zhao, Z. Wang, C. He, T. F. J. Poon, K. K. Pak, Y.-J. Liu, P. Ren, X.-J. Liu, and G.-B. Jo, Two-dimensional non-Hermitian skin effect in an ultracold Fermi gas, Nature (London) **637**, 565 (2025).
[21] T. Helbig, T. Hofmann, S. Imhof, M. Abdelghany, T. Kiessling, L. Molenkamp, C. Lee, A. Szameit, M. Greiter, and R. Thomale, Generalized bulk–boundary correspondence in non-Hermitian topolectrical circuits, Nat. Phys. **16**, 747 (2020).
[22] C. Lv, R. Zhang, Z. Zhai, and Q. Zhou, Curving the space by non-Hermiticity, Nat. Commun. **13**, 2184 (2022).
[23] C. Lv and Q. Zhou, Complexity geometry in Hermitian and non-Hermitian quantum dynamics, Phys. Rev. D **110**, 084039 (2024).
[24] Y.-J. Lin, K. Jiménez-García, and I. B. Spielman, Spin–orbit-coupled Bose–Einstein condensates, Nature (London) **471**, 83 (2011).
[25] Y.-J. Lin, R. L. Compton, A. R. Perry, W. D. Phillips, J. V. Porto, and I. B. Spielman, Bose-Einstein condensate in a uniform light-induced vector potential, Phys. Rev. Lett. **102**, 130401 (2009).
[26] Y.-J. Lin, R. L. Compton, K. Jimenez-Garcia, W. D. Phillips, J. V. Porto, and I. B. Spielman, A synthetic electric force acting on neutral atoms, Nat. Phys. **7**, 531 (2011).
[27] Here we use the saturation intensity suitable for the transition under consideration.

[28] C. Wang, N. Li, J. Xie, C. Ding, Z. Ji, L. Xiao, S. Jia, B. Yan, Y. Hu, and Y. Zhao, Exceptional nexus in Bose-Einstein condensates with collective dissipation, Phys. Rev. Lett. **132**, 253401 (2024).
[29] L. Pan, X. Chen, Y. Chen, and H. Zhai, Non-Hermitian linear response theory, Nat. Phys. **16**, 767 (2020).
[30] A. Ramanathan, S. R. Muniz, K. C. Wright, R. P. Anderson, W. D. Phillips, K. Helmerson, and G. K. Campbell, Partial-transfer absorption imaging: A versatile technique for optimal imaging of ultracold gases, Rev. Sci. Instrum. **83**, 083119 (2012).
[31] An equivalent sign change follows from swapping the frequencies of two Raman laser beams since $\mathcal{B} \propto p_0$.
[32] We note, however, that this antiunitary gauge transformation is incompatible with periodic boundary conditions.
[33] In this gauge, the interaction coefficient becomes spatially dependent, $g(x) = g\exp(2\mathcal{B}x/\hbar)$, leading to a position-dependent healing length ξ that slightly shifts $\langle x \rangle$ toward the edge with larger g.
[34] D.-W. Zhang, Y.-L. Chen, G.-Q. Zhang, L.-J. Lang, Z. Li, and S.-L. Zhu, Skin superfluid, topological Mott insulators, and asymmetric dynamics in an interacting non-Hermitian Aubry-André-Harper model, Phys. Rev. B **101**, 235150 (2020).
[35] K. Kawabata, K. Shiozaki, and S. Ryu, Many-body topology of non-Hermitian systems, Phys. Rev. B **105**, 165137 (2022).
[36] M. Zheng, Y. Qiao, Y. Wang, J. Cao, and S. Chen, Exact solution of the Bose-Hubbard model with unidirectional hopping, Phys. Rev. Lett. **132**, 086502 (2024).
[37] M. Albiez, R. Gati, J. Fölling, S. Hunsmann, M. Cristiani, and M. K. Oberthaler, Direct observation of tunneling and nonlinear self-trapping in a single bosonic Josephson junction, Phys. Rev. Lett. **95**, 010402 (2005).
[38] For these data, set the bias field to $B_0 = 670$ μT.
[39] W. M. Itano, D. J. Heinzen, J. J. Bollinger, and D. J. Wineland, Quantum Zeno effect, Phys. Rev. A **41**, 2295 (1990).
[40] Q. Zhou and W. Xu (private communication).
[41] L. M. Farrell, C. J. Howls, and D. H. J. O'Dell, Logarithmic catastrophes and Stokes's phenomenon in waves at horizons, J. Phys. A **56**, 044001 (2023).
[42] Y. Huang and B. Shklovskii, Anderson transition in three-dimensional systems with non-Hermitian disorder, Phys. Rev. B **101**, 014204 (2020).
[43] A. Tzortzakakis, K. Makris, and E. Economou, Non-Hermitian disorder in two-dimensional optical lattices, Phys. Rev. B **101**, 014202 (2020).
[44] L. Mao, Y. Hao, and L. Pan, Non-Hermitian skin effect in a one-dimensional interacting Bose gas, Phys. Rev. A **107**, 043315 (2023).
[45] R. Hamazaki, K. Kawabata, and M. Ueda, Non-Hermitian many-body localization, Phys. Rev. Lett. **123**, 090603 (2019).
[46] J. Tao, E. D. Mercado-Gutierrez, M. Zhao, and I. B. Spielman, Data for imaginary gauge potentials in a non-Hermitian spin-orbit coupled quantum gas, Zenodo, 2026, 10.5281/zenodo.18650354.
[47] See Supplemental Material at http://link.aps.org/supplemental/10.1103/tpfc-n3bq for experimental and data analysis methods, derivations of the imaginary gauge potential and the non-Hermitian equations of motion.